Spatially Resolved Crystalline and Amorphous Components of Polymeric Materials by Carbon-13 Chemical Shift Imaging Performed with Radio-Frequency Field Gradients

C. Malveau,[†] D. Grandclaude,[†] P. Tekely,[†] F. Beaume,[‡] and D. Canet*[,†]

Laboratoire de Méthodologie RMN (UPRESA CNRS 7042, INCM-FR CNRS 1742), Université H. Poincaré, Nancy I, B.P. 239, 54506 Vandoeuvre-lès-Nancy (Cedex), France, and Centre d'Etude, de Recherche et Développement d'ATOFINA (CERDATO), 27470 Serquigny, France

Received March 6, 2001

ABSTRACT: It is shown that chemical shift imaging can be easily adapted to high-resolution solid-state experiments by means of radio-frequency field gradient technology. (The gradient is delivered by a two-turn flat coil, the axis of which coinciding with the rotor axis.) The resulting two-dimensional diagram involves chemical shift information in one dimension and spatial information (along the rotation axis) in the other dimension. Different procedures (physical filters) have been considered in order to enhance specific properties of the crystalline and amorphous components in high-density polyethylene (hdpe). Two of them rely on differences in cross-polarization or in cross-polarization inversion processes, while a third one is based on carbon-13 longitudinal relaxation times. The latter is shown to be especially efficient for effectively obtaining separate images of the amorphous and crystalline components and ultimately unraveling their distribution within the sample. In particular, it is demonstrated that two structurally distinct amorphous phases are spatially separated in the sample under investigation.

Introduction

NMR imaging (and microscopy) has become a major tool in material science.[1] Concerning polymeric materials, the method can be dealt with in two different ways: either indirectly by imaging a solvent embedded in the material or directly by imaging the solid material itself. The former relies on the mobile components within the object under investigation and makes use of liquid-state imaging techniques. The latter is much more demanding with regard to spectroscopic methodology as, in that case, one is faced with the problem of lines broadened by internal anisotropic interactions, with however the benefit of obtaining genuine information devoid of any additional effect related to solvent uptake (swelling or more generally any kind of interaction between the solvent and the polymer). As we shall try here to detect possible heterogeneities that could be modified by solvent swelling, we shall resort to solid-state methods. The first task is obviously to choose a procedure, compatible with imaging techniques, for getting rid of line broadening due to dipolar couplings or other anisotropic interactions. Basically, two approaches can be thought of. The first one makes use of large-amplitude gradients capable of overcoming this line broadening[2] while the second one employs spectroscopic techniques[3] for removing (or attenuating) dipolar coupling effects. Even if proton NMR affords the best sensitivity, line narrowing is difficult, and despite a lower sensitivity, an interesting alternative is natural abundance carbon-13 spectroscopy provided that the following techniques are employed: (i) proton dipolar decoupling (DD) for removing dipolar couplings affecting the rare spin (carbon-13), (ii) magic angle spinning (MAS) for removing chemical shift anisotropy (CSA) effects, and (iii) cross-polarization (CP) for improving sensitivity. To carry out an NMR imaging experiment, field gradients are needed, and severe difficulties are encountered for synchronizing the gradient direction with sample rotation even though relatively slow spinning is employed.[4] Nevertheless, the only direction that is fixed is obviously the rotation axis, thus making it relatively easy to perform one-dimensional imaging. It turns out that, by contrast with static field gradient techniques,[4,5] radio-frequency (rf) field gradient techniques can be readily implemented for achieving such a goal.[6] They just require a flat coil, the axis of which coincides with the rotation axis, whereas the coil system needed in the case of static field gradients is somewhat more complicated.[7] Moreover, advantages of rf field gradients are well-known[8] in terms of very short rise and fall times and for their immunity to magnetic susceptibility variation effects. As a disadvantage of this approach, one must however note the necessity of minimizing the leakage between the gradient coil and the coil dedicated to normal spectroscopy operations. With respect to a previous report,[6] we are using here a probe that has been considerably improved regarding sensitivity and dipolar decoupling so that the method has become operational for attacking truly solid-state problems. In this respect, it must be stressed that NMR microscopy provides not only spin density images but also images contrasted by spectroscopic parameters[1] (relaxation times, chemical shifts, self-diffusion coefficients, etc.); maps of these parameters can eventually be obtained. The present study is precisely devoted to the separation (in terms of images) of the crystalline and amorphous components in a heterogeneous high-density polyethylene sample. Several types of discriminating procedures, prior the imaging procedure itself, have been considered in order to assess the spatial distribution corresponding to these two components.

Experimental Section

The material under investigation is a high-density polyethylene (hdpe) with density equal to 0.96. This is an industrial

[†] Université H. Poincaré.
[‡] Centre d'Etude, de Recherche et Développement d'ATOFINA.

10.1021/ma010409o CCC: $20.00
Published on Web 07/26/2001

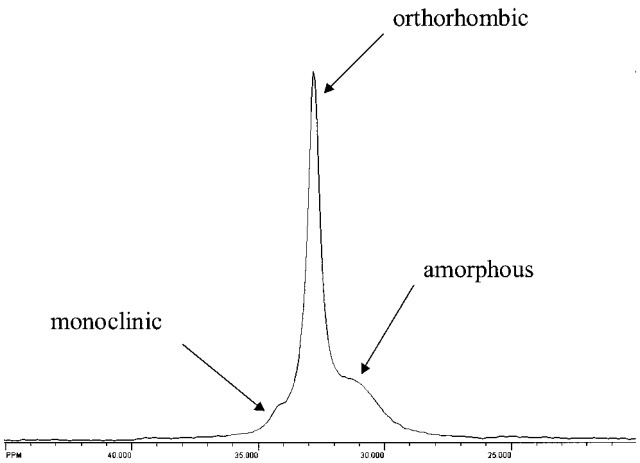

Figure 1. High-resolution 75 MHz CP/MAS/DD ^{13}C spectrum of high-density polyethylene powder. Cross-polarization time: 1 ms. Sample spinning frequency: 3 kHz.

product provided by Atofina (Serquigny, France). Its melt flow index is 7 g/10 mm at 190 °C under a weight of 2.16 kg. In such materials, the glass transition temperature is around −100 °C. A 3 mm thick plate was injection-molded, and for imaging experiments, a cylindrical sample was machined from this plate. The sample matches the inside of a Andrew type rotor so that the sides which have been in contact with the mold are perpendicular to the rotor axis which will be also the gradient axis, possible anisotropy being expected along that direction.

For standard high-resolution solid-state measurements, a Bruker DSX 300 spectrometer operating at 7 T (proton resonance frequency: 300 MHz) was used, and a standard CP/MAS ^{13}C spectrum is shown in Figure 1. It reveals the existence of two crystalline phases:[9] orthorhombic and monoclinic (which we will not attempt to differentiate in imaging experiments) and a partially resolved amorphous phase.

^{13}C chemical shift imaging experiments were performed with a homemade spectrometer[10] (proton resonance frequency: 200 MHz) built around a wide-bore (87 mm) Oxford magnet. The probe has been described previously;[6] several modifications in the tuning and matching circuits have greatly improved its performances regarding ^{1}H decoupling and ^{13}C sensitivity (amplifier power output of 140 and 800 W for ^{1}H and ^{13}C channels, yielding $\pi/2$ of 4.5 and 5 μs duration, respectively). The rf field gradient operates at the ^{13}C frequency (50 MHz) and is generated by a flat two-turn coil, the axis of which coincides with the rotor axis (achieving a gradient strength of 21 G/cm for a power amplifier output of 240 W). Because it must be electrically orthogonal to the coil devoted to normal spectroscopic operations, the latter is of the saddle type and must be doubly tuned to ^{1}H and ^{13}C frequencies with, on both channels, efficient stop circuits and capacitors able to stand high power. The basic sequence for spin density chemical shift imaging is sketched in Figure 2. The $\pi/2$ pulse applied to ^{13}C just after cross-polarization takes the magnetization toward the z axis, thus avoiding any phase setting between the gradient and spectroscopic channels (associated with the flat and saddle coils, respectively). This is followed by the application of the rf gradient for an incremented time t_1 such as a double Fourier transform with respect to t_1 and t_2 (t_2 being the dimension corresponding to normal acquisition), yielding a two-dimensional diagram with ^{13}C chemical shift information along the ν_2 frequency axis and spatial information (spin density) along the ν_1 frequency axis. A typical spectrum is shown in Figure 3 (horizontal and vertical axes correspond to ν_1 and ν_2, respectively). It exhibits the expected trace, indicating the location of the hdpe sample, but also a trace at the Delrin resonance corresponding to the rotor material and even a more extended trace showing the location of glue used for the probe fabrication.

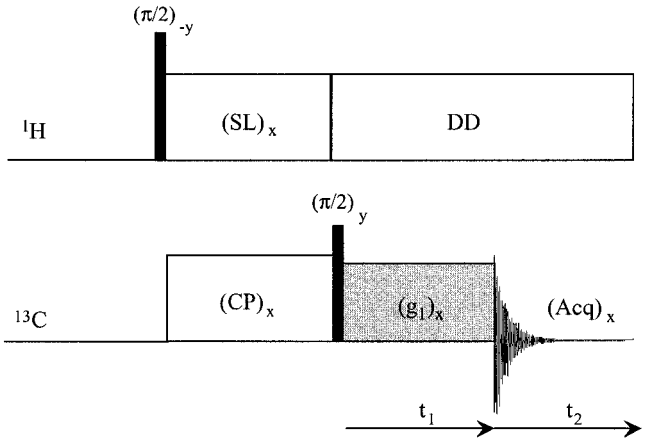

Figure 2. Basic pulse sequence used for ^{13}C chemical shift imaging. It differs from a classical CP/MAS/DD sequence by a $(\pi/2)_y$ pulse applied to ^{13}C subsequently to the cross-polarization stage (for taking ^{13}C magnetization to the z axis) followed by spatial encoding (application of a B_1 gradient pulse for a incremented time t_1) prior to the normal signal acquisition (t_2).

Spatial Discrimination of Crystalline and Amorphous Components

The objective of this work is to determine the spatial distribution of crystalline and amorphous components in an anisotropic polymeric material (this anisotropy arising from fabrication procedures). This can be achieved provided that we are able to separate these two components by means of a spectroscopic parameter. Good candidates arise for example from cross-polarization properties because ^{13}C spins in the crystalline component are expected to become polarized much more rapidly than in the amorphous component. Another possibility comes from the ^{13}C T_1 relaxation times because they are known to be drastically different in either phase. Different procedures, based on these features, are described below. They all exhibit the same trend, in a more or less straightforward manner, namely that the crystalline phase is uniformly distributed while the amorphous component is not. Also, it can be mentioned that relaxation actually takes place during application of the rf field gradient. However, this relaxation process is governed by a rate[8] equal to $(1/2)(1/T_1 + 1/T_2) \approx 1/2T_2$, which is roughly the same for all components, thus precluding any discrimination at this stage of the experiment.

Cross-Polarization Filter. In a general way, the dependence of the ^{13}C magnetization, M, as a function of the cross-polarization time contact time, t_c, may be described by a simplified equation[11]

$$M = M_0\lambda^{-1}(1 - e^{-\lambda t_c/T_{CH}})e^{-t_c/T_{1\rho}^{H}} \qquad (1)$$

where T_{CH} is the characteristic time of cross-polarization transfer, $T_{1\rho}^{H}$ is the proton rotating frame relaxation time, and $\lambda = 1 + T_{CH}/T_{1\rho}^{C} - T_{CH}/T_{1\rho}^{H}$, $T_{1\rho}^{C}$ being the ^{13}C rotating frame relaxation time. Because $T_{1\rho}^{C} \gg T_{1\rho}^{H}$, λ reduces to $\lambda = 1 - T_{CH}/T_{1\rho}^{H}$. Experimental data ($^{13}C$ magnetization as a function of t_c; not shown) can be fitted according to eq 1 and to the proportion of rigid (including monoclinic and orthorhombic crystalline phases) and mobile components. Results are given in Table 1. It can be recalled that for typical organic systems, at long contact times, the cross-polarization

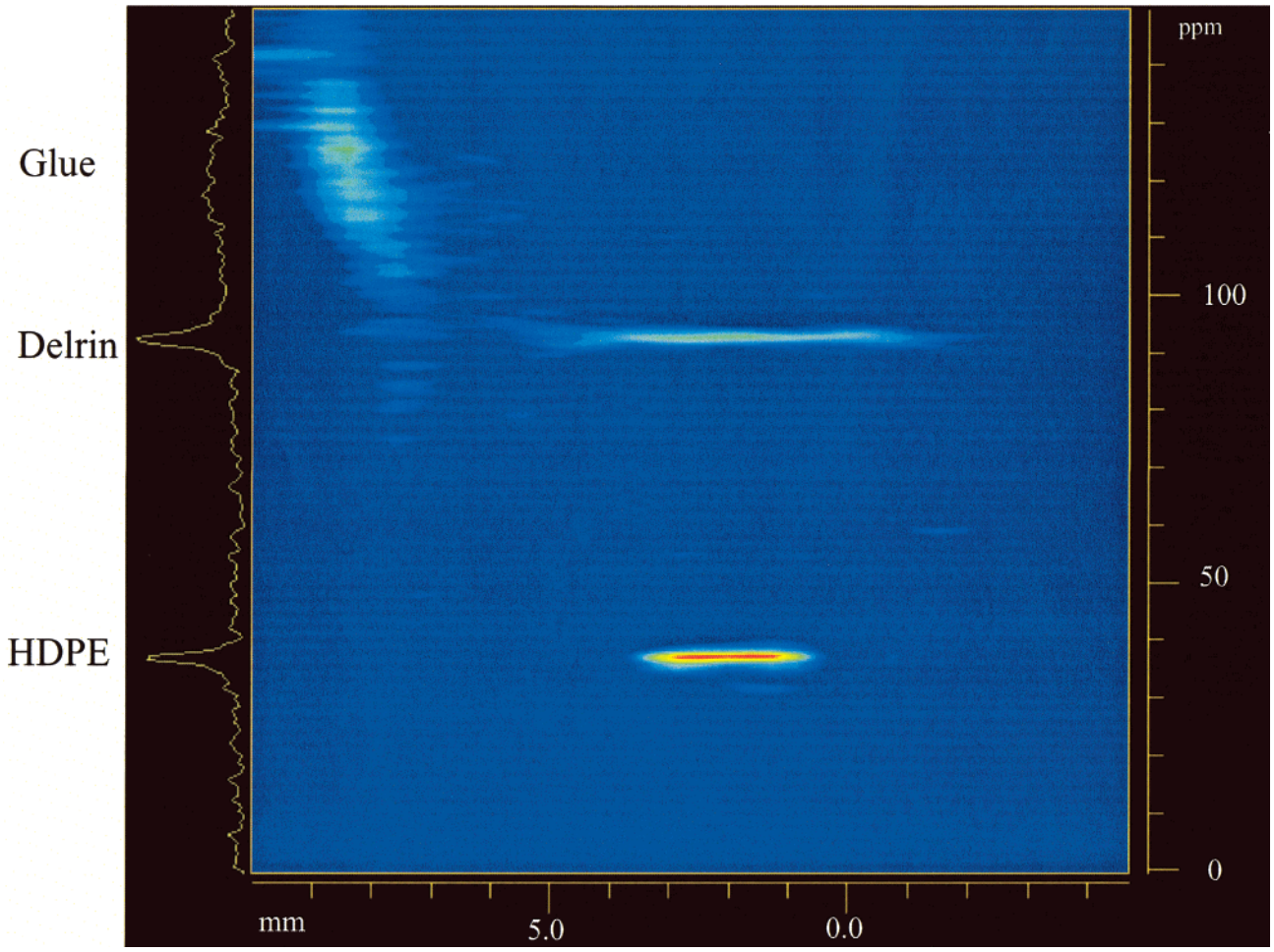

Figure 3. Typical ^{13}C chemical shift image (according to the experiment of Figure 2) of a hdpe cylinder (of 3 mm height) placed in a Delrin rotor; the trace corresponding to the latter surrounds the hdpe trace, as expected. Also visible are signals arising from ^{13}C-containing materials (presumably glue used for the probe construction). The following parameters were used. Spinning frequency: 3 kHz; cross-polarization time: 5 ms; 400 transients for each of the 32 t_1 increments, separated by a recycle time of 5 s. t_1 is incremented in 10 μs steps. A complex Fourier transform is performed in the t_2 dimension (signals acquired in the quadrature mode), and after phase correction, its real part is subjected to a single zero-filling followed by a real Fourier transform (t_1 dimension).

Table 1. Parameters Deduced from the Analysis of Cross-Polarization vs Contact Time

component	%	T_{CH} (μs)	$T_{1\rho}^{H}$ (ms)
mobile	34	200	10
rigid[a]	66	20	90

[a] Including the crystalline phase and the intermediate rigid amorphous component.

curve is dominated by $T_{1\rho}^{H}$, whereas T_{CH} is the dominant factor of the initial part. Owing to a difference by an order of magnitude in T_{CH}, this means that, at short contact times, ^{13}C nuclei in the rigid component will be more polarized than in the mobile component, hence a possible preview (although not quantitative) of the spatial distribution corresponding to both components. This is indeed observed in Figure 4 where a slight nonuniformity of profiles seems to be above the noise level and shows up a somewhat higher intensity for their rightmost part. This feature can be explained if we postulate the presence of a greater amount of rigid component (including the crystalline and a rigid intermediate component, see below) preferentially located in the part of the sample appearing on the right-hand side. However, the lack of separate images for the two components prevents definite conclusions, and other parameters have to be explored.

Cross-Polarization Inversion Filter. When cross-polarization transfer has been completed, it proves possible either to cancel this transferred polarization or even to invert it by shifting by 180° the phase of the proton spin-lock field while maintaining the contact between abundant and rare spin reservoirs[12] (see Figure 5). As the process following polarization transfer is still governed by T_{CH}, ^{13}C in the rigid phases get depolarized much faster than in the mobile phase. This is illustrated in Figure 6 where it can be seen that, for a cross-polarization inversion time, the signals corresponding to the crystalline and amorphous components have been inverted or canceled. These features suggest a simple procedure for separating the NMR signal from rigid (mostly crystalline) and mobile components: the sum of two imaging experiments—one without inversion and the other with the appropriate cross-polarization inversion—should yield the mobile amorphous component profile while their subtraction involves twice the rigid component in addition to the mobile component with its normal amplitude. Profiles shown in Figure 7 have been obtained along these lines. The actual depolarization time leading to an optimized image (in terms of inversion of the crystalline contribution and cancellation of the amorphous contribution) is significantly longer than the one derived from experiments carried out at 7 T on the standard CP/MAS 7 mm probe; this is due to

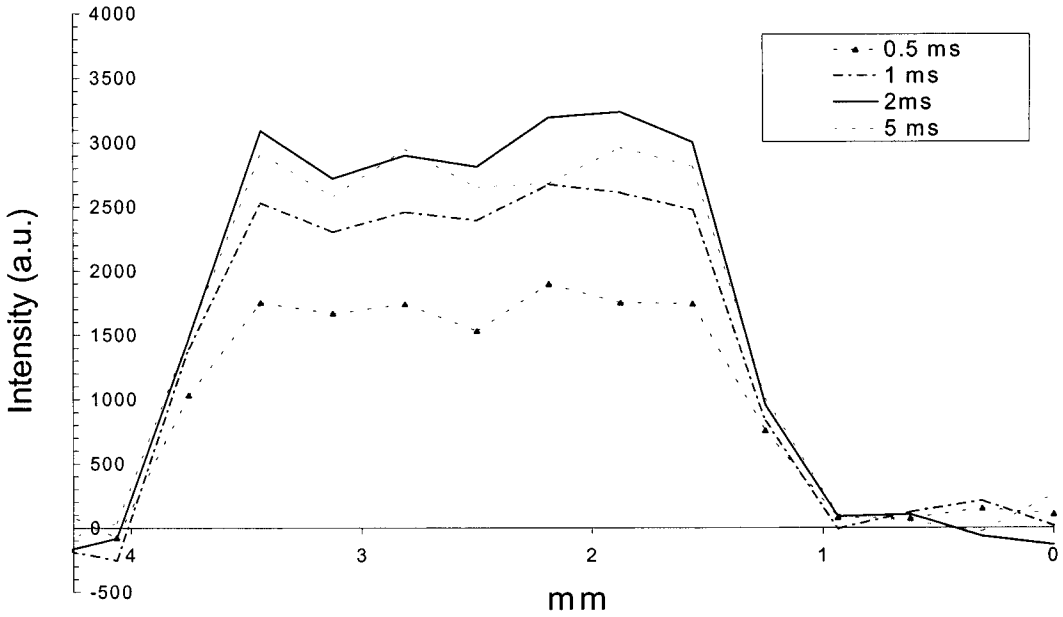

Figure 4. Profiles as a function of the cross-polarization time (given in the inset), obtained from an image of the same type as the one of Figure 3 by summing the cross sections corresponding to the chemical shift zone of hdpe. Same experimental conditions as for Figure 3 except that t_1 is incremented in 25 μs steps for improving the digital resolution in the ν_1 dimension. Also, the carrier frequency has been set at 500 Hz from the hdpe resonance so as to avoid image distortions by off-resonance effects.

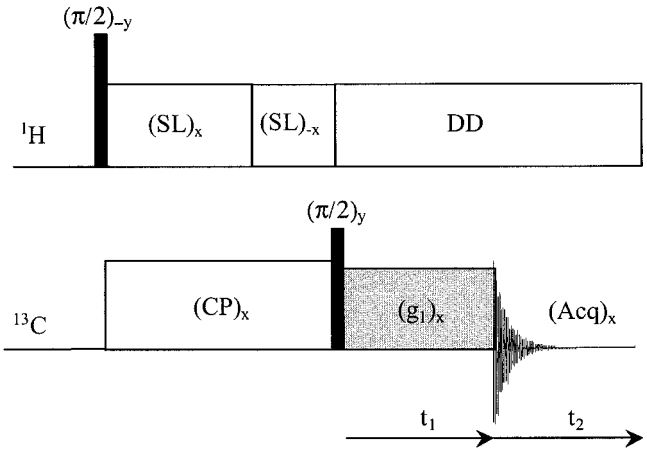

Figure 5. Pulse sequence used for chemical shift imaging with a polarization-inversion filter. It differs from the basic sequence of Figure 2 by a phase reversing of the proton irradiation in the last part of the cross-polarization stage.

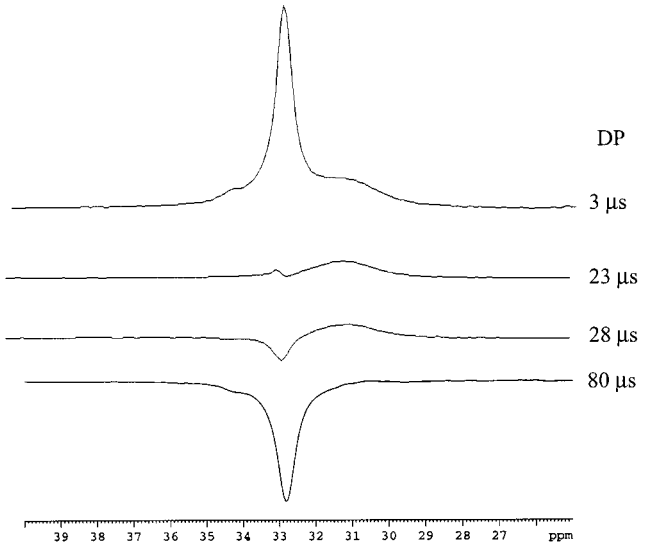

Figure 6. Examples of polarization-inversion spectra obtained with the 7 T spectrometer (measurement frequency: 75 MHz; see Figure 1) for different values of the depolarization time DP corresponding to $(SL)_{-x}$ in Figure 5. (Of course, the actual sequence used for these experiments does not involve the space encoding stage.) The polarization time, $(SL)_x$ of Figure 5, was set to 1 ms. For an appropriate depolarization time (here DP = 80 μs), the signal of the amorphous phase from the rightmost part of the spectrum has virtually disappeared, whereas the orthorhombic and monoclinic signals are essentially inverted.

different geometrical and electronic characteristics of the corresponding probes. Nevertheless, the important point is the nonuniform distribution of the mobile amorphous component, as clearly observed in its specific profile. It can be noticed that its deficiency in the right part of the sample corroborates the cross-polarization experiments (see Figure 4). Concerning the "rigid" profile, it must be borne in mind that it actually involves twice the rigid components plus the mobile component with its normal amplitude. As the latter presents a deficiency in the right part of the profile while the rigid part exhibits a slight excess in the same region, both effects cancel, leading to a uniform intensity for this "rigid" profile. However, we will show that the filter used in the next section leads to a better visualization of the various components existing within the sample.

^{13}C Longitudinal Relaxation Time Filter. Although proton relaxation times in the rotating frame would be good candidates for a convenient discrimination between crystalline and amorphous components, they turned out to be of little use in practice since they would imply the application of radio-frequency fields for relatively long periods and thus prone to induce probe alterations. It appeared therefore wiser to turn to parameters not implying application of long spin-locking fields, namely transverse or longitudinal relaxation times. Among them, ^{13}C longitudinal relaxation times seem most suitable because their values for crystalline and amorphous components differ by at least 1 order of magnitude. The first step is to ascertain that these parameters are sufficiently discriminating; they have therefore been measured at 7 T using the conventional

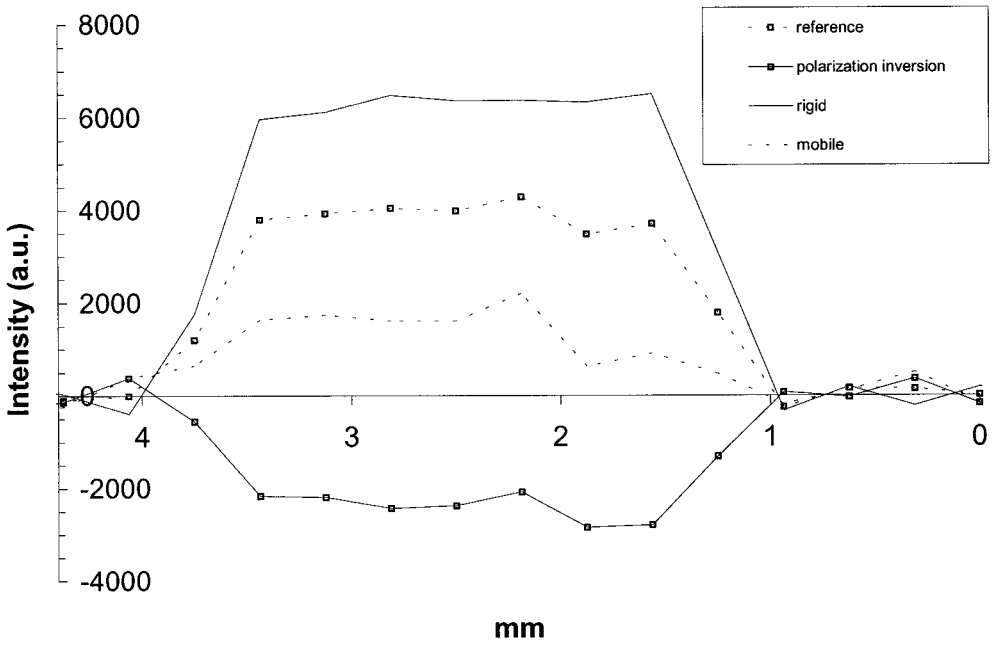

Figure 7. Profiles obtained under similar conditions as for Figures 3 and 4. The reference and polarization-inversion profiles correspond to polarization-inversion times of 1 and 250 μs (polarization time: 5 ms), respectively (see Figure 5). The "rigid" profile is affected, in part, by a contribution from the mobile component (see text).

Table 2. ^{13}C Longitudinal Relaxation Times and Relative Proportions of the Amorphous, Intermediate, and Crystalline (Monoclinic and Orthorhombic) Components As Deduced from the Experiments Performed at 7 T (See Text)

component	%	T_1 (s)
amorphous I	32	0.45
amorphous II (intermediate)	15	30
crystalline	53	801

method[13] which consists of applying the cluster ($\pi/2-\tau-\pi/2$) subsequently to the cross-polarization stage. The first $\pi/2$ pulse takes the ^{13}C magnetization toward the z axis. It then evolves to its equilibrium value during the interval τ, and the longitudinal magnetization is converted into an observable signal by means of the second $\pi/2$ pulse and finally detected. The experiment is repeated for a series of τ values which yield the longitudinal relaxation times. Because amorphous and crystalline signals strongly overlap, the area of the whole resonance has been monitored as a function of τ, yielding a multiexponential behavior. In our case, three exponentials could be identified, leading to the longitudinal relaxation times of the three components, together with their relative proportions. Results of this analysis are reported in Table 2. The shortest and largest relaxation times can be assigned unambiguously to mobile amorphous and crystalline (monoclinic and orthorhombic) phases, respectively. The value of 30 s arises from an "intermediate" phase. The large differences in T_1 values suggest a straightforward discrimination between crystalline components and the amorphous components. As far as chemical shift imaging is concerned, this can be achieved by the sequence depicted in Figure 8. The aim of the ^{13}C $\pi/2$ pulse is to take the magnetization either to $+z$ (first part of the sequence) or to $-z$ (second part of the sequence). Longitudinal magnetization is then allowed to evolve during the interval τ which is chosen so that magnetization of the amorphous part reaches its thermal equilibrium value, whereas the one of crystalline components is essentially

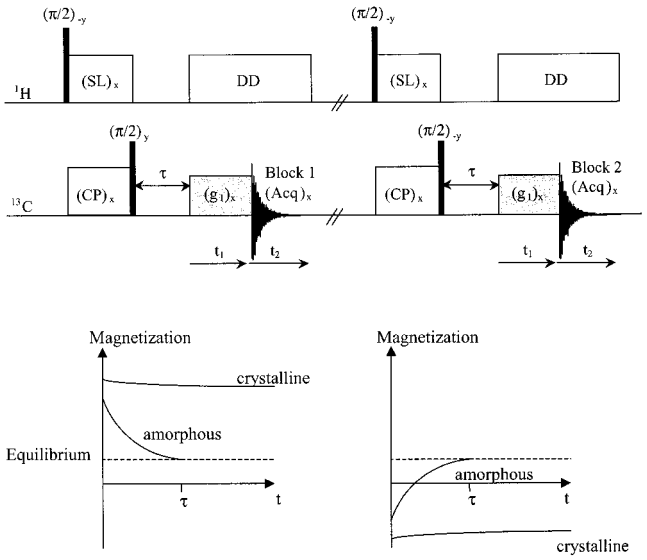

Figure 8. (top) Pulse sequence used for discriminating amorphous and crystalline components according to their ^{13}C T_1 values. Experiments are performed in alternate blocks so as to minimize effects of instrumental drifts. Experimental parameters are those of Figures 3 and 4 (except that 1200 transients are accumulated for each t_1 increment) with $\tau = 4$ s. (bottom) Sketch of the magnetization evolution of both components (T_1(crystalline) $\gg$ T_1(amorphous)) in blocks 1 and 2 (left and right, respectively).

unchanged due to the large difference in longitudinal relaxation times (see Figure 8, bottom). Thereafter, spatial encoding takes place, and the resulting fids are stored in two different memory blocks for further data manipulation. These two parts of the experiment are interleaved in order to minimize effects of instrumental drifts. From Figure 8 (bottom), it is easy to see that addition of the two blocks will yield the chemical shift image of the amorphous components while subtraction leads exclusively to the crystalline components. The results are displayed in Figure 9 in the form of two-

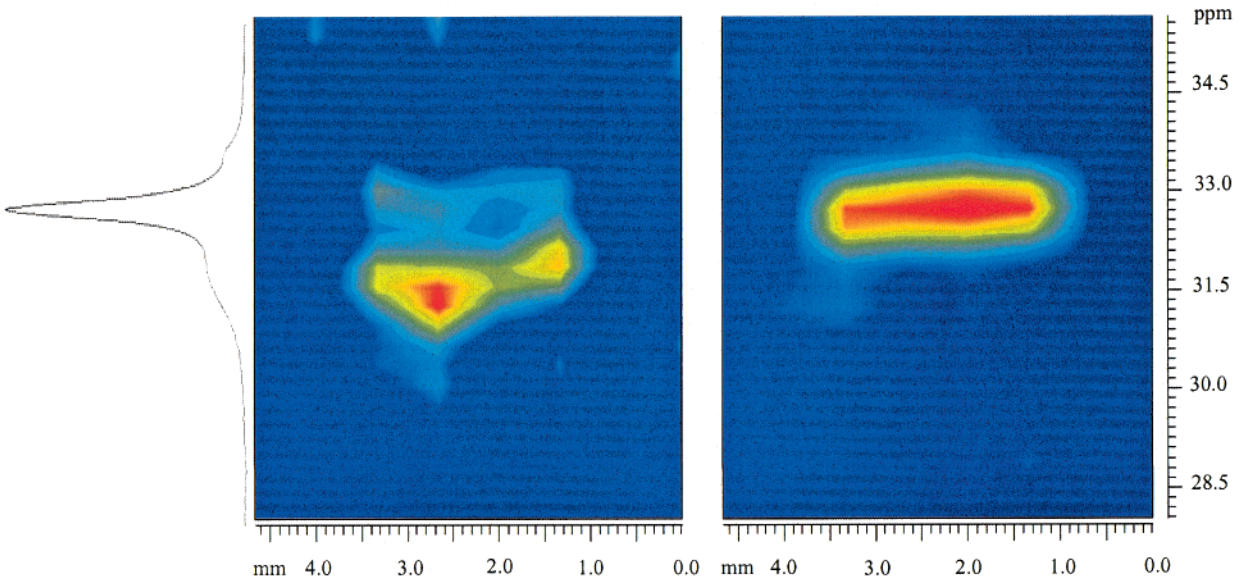

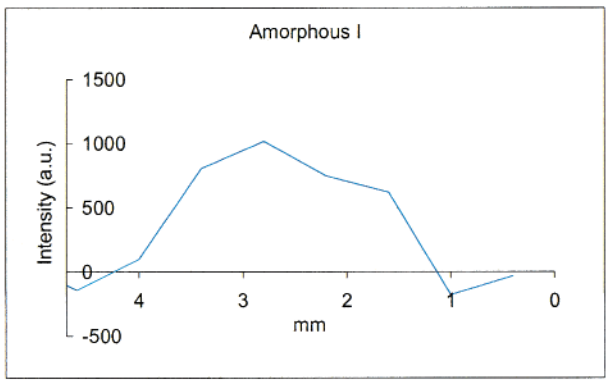

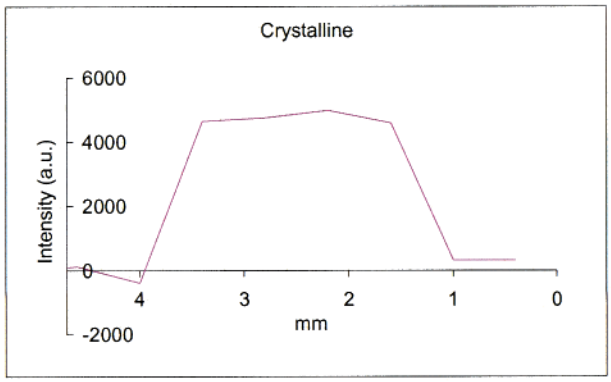

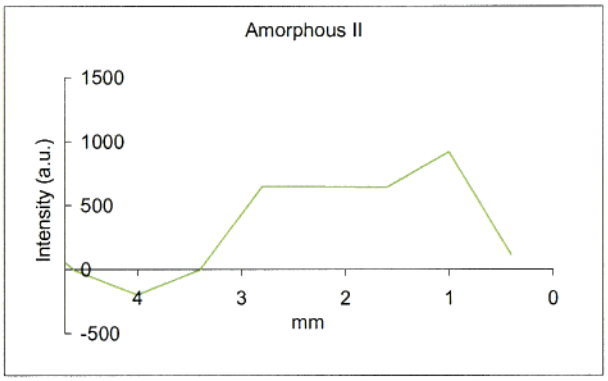

Figure 9. (top) Chemical shift imaging diagrams obtained by adding and subtracting blocks 1 and 2 of the sequence depicted in Figure 8. The left and right diagrams correspond to the amorphous and crystalline components, respectively. Notice that chemical shift increases from bottom to top, while in Figure 1, it increases from right to left. (bottom) Cross sections extracted from the two-dimensional diagrams at the chemical shift corresponding to maximum intensity: on the right (crystalline) taken through the right image; on the left taken through the left image at 31.5 ppm (amorphous I) and 32.0 ppm (amorphous II).

dimensional diagrams and in the form of cross sections, each of them associated with a characteristic chemical shift. These cross sections (although suffering from a relatively low signal-to-noise ratio) confirm the conclusions drawn from the cross-polarization and polarization-inversion experiments: the crystalline component is roughly uniform over the whole sample whereas the amorphous component is apparently nonuniform as it exhibits an over-intensity at the left and right sides of the sample (more pronounced in the left side). To fully understand the nature and origin of this nonuniformity, we can better rely on the two-dimensional diagram (Figure 9, left) corresponding to the amorphous component. (This was not possible with the polarization and polarization-inversion experiments, due to spectra of lower quality.) It can be seen that the density variations

go together with small chemical shift changes, indicating that the amorphous component possesses different structural (conformational) features according to its location within the sample. We wish to point out that, besides the conventional crystalline (rigid) and amorphous (mobile) phases, ^{13}C T_1 experiments have revealed the existence of an intermediate phase which could be an amorphous phase involving more rigidity (tie molecules, loops, interfacial chains, etc.) which exists in polyethylene.[14−18] This phase should be related to the rightmost part of the amorphous image and will be denoted amorphous II. As the right part of the amorphous image corresponds precisely to chemical shift close to the one of the orthorhombic phase, this indicates that chains in the intermediate phase have similar conformation. Now, because the ^{13}C longitudinal relaxation time in this amorphous II phase is longer than for the mobile amorphous phase (dubbed amorphous I), the relevant intensity will be lowered due to the particular preparation based precisely on longitudinal relaxation time values with respect to the evolution interval τ. The value of 30 s found at 75 MHz (7 T) for the intermediate phase T_1 is presumably overestimated due to the multiexponential treatment (which is known to entail large uncertainties) and is probably lower at 50 MHz. Anyhow, a clear visualization of two different amorphous components (in the right and left parts of the sample, respectively) is consistent with the experimental observations based on cross-polarization and polarization inversion, since the more rigid component (located preferentially in the right part) will get polarized faster than the mobile one. The next step is to explain why such a difference in the location of two distinct amorphous phases can exist. This can be related to the way of preparing the hdpe sample which is of injection-molded type. One possibility arises from different cooling conditions on the two sides of the mold, entailing different structural properties for the amorphous phases at the level of the two sample sides. Further and deeper insight into the phase structure of injection molded hdpe will be necessary to explain fully the observed effects.

Conclusion

The technique of ^{13}C chemical shift imaging in rotating solids by radio-frequency gradients has been improved to such an extent that it can be applied to structural studies of polymeric materials. One advantage of the method lies in the possibility of using a spectroscopic property in order to separate amorphous and crystalline components. Several variants could be considered; among them, in the present work, ^{13}C longitudinal relaxation times turned out to be the parameter of choice for obtaining detailed phase structure information. The power of ^{13}C chemical shift imaging by radio-frequency field gradients is well demonstrated by the fine visualization of two spatially nonuniform amorphous components related to the fabrication process. Such a potentiality makes valuable the experimental method, which is relatively simple and little demanding on the instrumental side and could be easily extended to numerous studies in the field of material sciences, including the spatial effects of mechanical constraints, aging, and other chemical transformations.

References and Notes

(1) Blümich, B. *NMR Imaging of Materials*; Clarendon Press: Oxford, 2000.
(2) Demco, D. E.; Blümich, B. *Concepts Magn. Reson.* **2000**, *12*, 188.
(3) Demco, D. E.; Blümich, B. *Concepts Magn. Reson.* **2000**, *12*, 269.
(4) Scheler, U.; Schauss, G.; Blümich, B.; Spiess, H. W. *Solid State NMR* **1996**, *6*, 375.
(5) Nonaka, M.; Matsui, S.; Inouye, T. *J. Magn. Reson.* **2000**, *145*, 315.
(6) Malveau, C.; Diter, B.; Tekely, P.; Canet, D. *J. Magn. Reson.* **1998**, *134*, 171.
(7) Maas, W. E.; Bielecki, A.; Ziliox, M.; Laukien, F. H.; Cory, D. G. *J. Magn. Reson.* **1999**, *141*, 29.
(8) Canet, D. *Prog. NMR Spectrosc.* **1997**, *30*, 101.
(9) Mathias, L. J. *Solid State NMR of Polymers*; Plenum Press: New York, London, 1991.
(10) Maffei, P.; Mutzenhardt, P.; Retournard, A.; Diter, B.; Raulet, R.; Brondeau, J.; Canet, D. *J. Magn. Reson.* **1994**, *A107*, 40.
(11) Mehring, M. *Principles of High-Resolution NMR in Solids*; Springer: Berlin, 1983.
(12) Cory, D. G.; Ritchey, W. M. *Macromolecules* **1989**, *22*, 1611.
(13) Torchia, D. A. *J. Magn. Reson.* **1978**, *30*, 613.
(14) VanderHart, D. L.; Khoury, F. *Polymer* **1984**, *25*, 1589.
(15) Ando, I.; Sorita, T.; Yamanobe, T.; Komoto, T.; Sato, H.; Deguchi, K.; Imanari, M. *Polymer* **1985**, *26*, 1864.
(16) Cholli, A. L.; Ritchey, W. M.; Koenig, J. L.; Veeman, W. S. *Spectrosc. Lett.* **1988**, *21*, 519.
(17) Nakagawa, M.; Horii, F.; Kitamaru, R. *Polymer* **1990**, *31*, 323.
(18) Chen, Q.; Yamada, T.; Kurosu, H.; Ando, I.; Shiono, T.; Doi, Y. *J. Polym. Sci., Part B: Polym. Phys.* **1992**, *30*, 591.

MA010409O